Signatures of Hund metal and finite-frequency nesting in Sr_2RuO_4 revealed by electronic Raman scattering

Germán Blesio [1,2,*] Sophie Beck [3] Olivier Gingras [3] Antoine Georges [4,3,5,6] and Jernej Mravlje [1,7]

[1]*Jožef Stefan Institute, Jamova 39, SI-1000 Ljubljana, Slovenia*
[2]*Instituto de Física Rosario (CONICET) and Facultad de Ciencias Exactas, Ingeniería y Agrimensura, Universidad Nacional de Rosario, 2000 Rosario, Argentina*
[3]*Center for Computational Quantum Physics, Flatiron Institute, New York 10010, USA*
[4]*Collège de France, 11 place Marcelin Berthelot, 75005 Paris, France*
[5]*CPHT, CNRS, Ecole Polytechnique, Institut Polytechnique de Paris, Route de Saclay, 91128 Palaiseau, France*
[6]*Department of Quantum Matter Physics, University of Geneva, 24 quai Ernest-Ansermet, 1211 Geneva, Switzerland*
[7]*Faculty of Mathematics and Physics, University of Ljubljana, Jadranska 19, 1000 Ljubljana, Slovenia*

(Received 26 April 2023; accepted 1 April 2024; published 3 May 2024)

We investigate the electronic Raman scattering of Sr_2RuO_4 using a material-realistic dynamical mean-field theory approach. We identify the low-energy Fermi liquid behavior and point out that the enhanced Raman response at higher energies is a fingerprint of Hund metals. These signatures originate in the two-stage coherence of Hund metals and associated quasiparticle "unrenormalization." In agreement with recent experimental observations, we find the B_{1g} and B_{2g} responses differ, but our calculations suggest a novel interpretation of this dichotomy. The B_{1g} response is dominated by the xy orbital and the B_{2g} response receives contributions from all orbitals and is strongly affected by previously unnoticed finite-frequency interband nesting. We calculate the vertex-corrections to Raman response and show that their effect is nonvanishing but small.

DOI: 10.1103/PhysRevResearch.6.023124

I. INTRODUCTION

Raman inelastic light scattering is a powerful probe of molecules and materials. Raman shifts and scattering intensities reveal vibrational modes, providing invaluable insights into molecules and compounds relevant to chemistry, biology, and materials science [1]. Electrons in materials scatter light inelastically too, and the associated electronic Raman response [2] has been used to characterize the pseudogap and superconducting phases of cuprates [3–5], the nematicity in pnictides [6–8] and to document strange-metal behavior and quantum criticality [9,10], to name only a few. An important advantage of Raman scattering is that by varying the polarization of the incident and reflected light one can probe different symmetry sectors and access the momentum dependence of the scattering.

Theoretically, Raman scattering has been investigated with weak coupling approaches [11,12] and, for strongly correlated models, with dynamical mean-field theory [2,13–18] and determinantal quantum Monte Carlo [19]. Whereas phonon frequencies and associated Raman shifts are routinely calculated [20,21], electronic Raman scattering is rarely considered and has been evaluated for a few cases only [22,23]. The rarity of material-realistic approaches represents a significant hindrance to the interpretation of experiments, highlighting the need for further work in this area. Our paper develops such an approach and applies it to a case of great current interest, the layered ruthenate compound Sr_2RuO_4.

The motivation for our investigation is Ref. [24] that recently reported experimental measurements of the electronic Raman response in Sr_2RuO_4. The much discussed Sr_2RuO_4 compound is a multiorbital layered unconventional superconductor [25] displaying Fermi liquid behavior below a low quasiparticle coherence scale (e.g., resistivity $\propto T^2$ below $\sim$25 K). On a broader energy and temperature range, Sr_2RuO_4 has been characterized [26–28] as a Hund metal [29,30]. A hallmark of Hund metals is that local orbital fluctuations become quenched at a distinctly higher energy scale than local spin fluctuations [27,31–34]. This two-stage screening leads to a distinctive non-Fermi liquid feature at a characteristic intermediate energy scale in the one-particle spectral function and self-energy [33,35–37]. Another hallmark of Hund metals is a tendency towards orbital differentiation, manifested by distinct values of quasiparticle renormalizations in bands spanned by different orbitals. In Sr_2RuO_4 the broader quasi-two-dimensional γ-band, predominantly spanned by the xy-orbital and displaying a van Hove singularity close to Fermi level, is more renormalized (i.e., it has a higher mass enhancement $\sim$5–6 compared to band theory) [25,26] than the α/β quasi-one-dimensional sheets spanned by the xz/yz orbitals (mass enhancement $\sim$3.5).

*blesio@ifir-conicet.gov.ar

In Ref. [24], they measured the Raman spectra in different channels, found a less coherent response in the B_{2g} channel, and interpreted the dichotomy between the B_{1g} and the B_{2g} response in terms of the orbital effects, referring to the effect as the 'orbital-dichotomy'. This interpretation may appear natural since a simple approximation $\sim\partial^2\epsilon(\mathbf{k})/\partial k_x\partial k_y$ to the Raman vertex in this channel suggests that it is insensitive to the more coherent quasi-one-dimensional α/β bands, leading to the interpretation [24] that the B_{2g} response may originate dominantly from the xy orbital and the B_{1g} channel from the xz/yz ones. However, the quasiparticle response reported for the B_{2g} channel is quite faint even at low T [24], which seems at odds with Fermi liquid behavior and raises questions about the appropriate interpretation. What are the signatures associated with the Fermi liquid regime and those associated with the higher energy non-Fermi liquid Hund metal effects? How does the orbital differentiation manifest itself in the Raman response? These questions can only be convincingly addressed theoretically in a materials-realistic approach.

Here, we answer these questions by calculating and analyzing the electronic Raman response of Sr_2RuO_4 in a dynamical mean-field theory (DMFT) framework based on first-principles density-functional theory (DFT) electronic structure. The Raman vertices are calculated in a matrix-valued effective mass approximation. By comparison with simplified model calculations we disentangle the Fermi liquid response from the higher-energy non-Fermi liquid response and show that the latter reveals characteristic spectral features of Hund metals. We also investigate why the Raman responses in the B_{1g} and B_{2g} channels differ. We show that, in contrast to the interpretation of Ref. [24], the B_{1g} channel is dominated by the xy orbital and find that the B_{2g} response displays a spectral feature associated with the enhancement of inter-band contributions by an interesting finite-frequency nesting property.

II. METHODS

We perform DFT+DMFT calculations for a DFT-derived Wannier Hamiltonian [38] spanning the t_{2g} bands of Sr_2RuO_4 as described in Ref. [39], taking into account the correlation-enhanced spin-orbit coupling $\sim$0.2 eV [40,41]. We use the hybridization-expansion quantum Monte Carlo solver from the TRIQS software library [42–45], using the interaction parameters $U = 2.3$ eV and $J = 0.4$ eV, which were originally estimated from constrained-RPA calculations [26] and shown to give results consistent with several experimental observables [26–28,39,46–49]. The Matsubara self-energies are continued to real-frequency using Padé interpolation. We checked that the results do not change significantly if we use Maximum Entropy analytical continuation. The Raman response is given by (in units where $e^2 = 1$ and $\hbar = 1$):

$$\chi''_\mu(\Omega) = \pi \sum_{\mathbf{k}} \int d\omega \big\{ [f(\omega) - f(\omega+\Omega)] \times \mathrm{Tr}\, \gamma^\mu_{\mathbf{k}}\, \mathcal{A}_{\mathbf{k}}(\omega)\, \gamma^\mu_{\mathbf{k}}\, \mathcal{A}_{\mathbf{k}}(\omega+\Omega) \big\}. \quad (1)$$

In this expression, both the Raman vertex $\gamma^\mu_{\mathbf{k}}$ in channel μ and spectral functions $\mathcal{A}_{\mathbf{k}}$ at momentum $\mathbf{k}$ are 6×6 matrices in spin and orbital space; $f(\omega)$ is the Fermi function. In Eq. (1) we retained only the so-called bubble contributions to the response [50]. It is well known that for the case of optical conductivity the vertex corrections vanish in DMFT due to the oddness of the velocity matrix elements upon inversion for centrosymmetric systems [13,51]. This argument does not hold however for the Raman response, because the Raman matrix elements transform differently. In Appendix H we show that (i) when the interband terms are neglected, the vertex corrections in the considered channels vanish by reflection symmetries, and (ii) numerically test that their contribution remains small even when the interband terms are included. Following Ref. [23], we calculate the Raman vertices in a matrix valued effective mass approximation generalizing the approach of Ref. [52]:

$$\left[\gamma^\mu_{\mathbf{k}}\right]_{\nu\nu'} = \sum_{\alpha\beta} e^i_\alpha \frac{\partial^2 H^{(W)}_{\nu\nu'}}{\partial k_\alpha \partial k_\beta} e^s_\beta, \quad \nu,\nu' \text{ band indices},$$

$$\gamma^{B_{1g}}_{\mathbf{k}} = \frac{1}{2}\left(\frac{\partial^2 H^{(W)}}{\partial k_x^2} - \frac{\partial^2 H^{(W)}}{\partial k_y^2}\right), \quad \gamma^{B_{2g}}_{\mathbf{k}} = \frac{\partial^2 H^{(W)}}{\partial k_x \partial k_y}, \quad (2)$$

expressed in terms of the second derivative of the Wannier Hamiltonian $H^{(W)}$ with respect to $\mathbf{k}$ (in a direction related to the polarization of the incoming/scattered light e^i and e^s). We emphasize that, importantly, this expression includes intraband and interband contributions. The derivatives were performed as outlined in Ref. [53] using the Wannier interpolation as implemented in the WannierBerri library [54,55]. We use a $60\times 60\times 60$ Monkhorst-Pack grid to sample the Brillouin zone, which we verified to be sufficient for convergence.

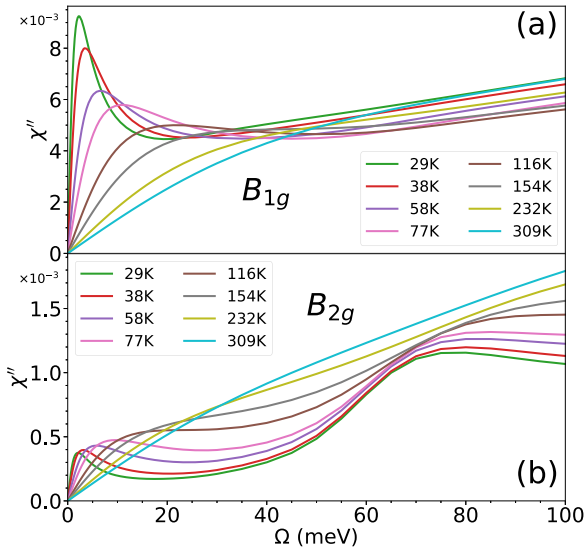

FIG. 1. Raman response in B_{1g} (top panel) and B_{2g} (bottom panel) channels for different temperatures. The susceptibilities are expressed in atomic units (i.e., setting the prefactor $e^2/(\hbar a_0 m_e)$ equal to unity).

III. RESULTS

Figure 1 displays the temperature (T) and frequency dependence of the calculated Raman responses. The top panel depicts the results in the B_{1g} channel. For low T, one sees a low-frequency Drude peak that is followed by a moderate

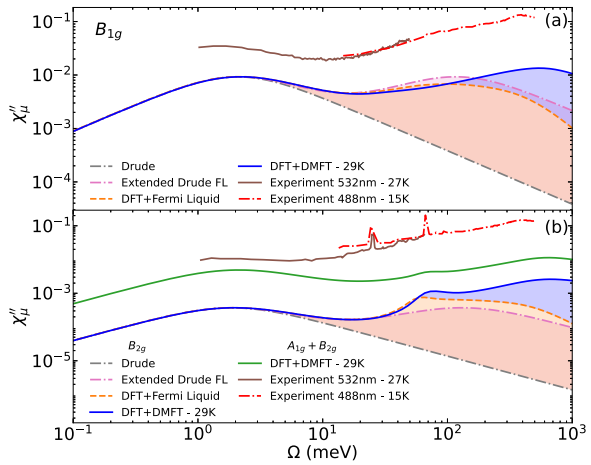

FIG. 2. Raman response for the B_{1g} (a) and B_{2g} (b) channel. In addition to the full DFT+DMFT result at $T = 29$ K (solid blue line), we also display a calculation where the DMFT self-energy for each orbital is replaced by a Fermi liquid expression consistent with its low-energy behavior (orange dashed). The results are compared to: a simple Drude fit with an optical scattering rate $\Gamma^* = \text{const.}$ (gray dashed-dotted) and an extended Drude fit with a Fermi liquid optical scattering rate $\Gamma^* \propto \Omega^2 + (2\pi k_B T)^2$ (pink dashed-dotted). We also display the experimental results from Refs. [24] and [58] (shifted away vertically for clarity). On the bottom panel, the same curves are plotted for B_{2g}, except for the experimental data which are currently available in a broader frequency range only for the A_{1g}+B_{2g} channel [24,58]. For direct comparison, we also plot the DFT+DMFT results for that channel (green). See Appendix G for the expression of the Raman vertex in the A_{1g}+B_{2g} channel.

increase at a higher frequency, a dependence that is characteristic of the Fermi liquid coherent response [24,56,57]. This dependence persists up to $T \sim 200$ K. For higher T the peak-dip-increase structure is lost and one observes only a monotonous increase with frequency in the presented frequency range.

In the B_{2g} channel shown in Fig. 1(b), one also sees a Drude peak but its intensity is smaller compared to an additional feature that takes the shape of a peak centered around 80 meV at low T. The intermediate minimum disappears at a somewhat lower T than observed in the B_{1g}. At $T \sim 100$–150 K in B_{2g}, the two-peak structure transforms to that of a plateau followed by a steeper increase, whereas in B_{1g} this growth of the response above 40 meV remains mild. Qualitatively similar features, also with a smaller overall intensity but with a steeper increase with frequency in the B_{2g} case, was also observed in experiments [24].

In Fig. 2, we display the calculated low temperature $T = 29$ K spectra in a broader energy range. To gain insight into the different features of the spectra, we also display (i) a simple low-energy Drude fit $\chi'' \propto \omega/(\omega^2 + \Gamma^{*2})$ with constant scattering rate Γ^*, (ii) an extended Drude fit using a frequency-dependent Fermi liquid scattering rate $\Gamma^*(\omega) \propto [\omega^2 + (2\pi k_B T)^2]$, and (iii) a "DFT+Fermi liquid" approximation in which the DMFT self-energies have been replaced by their low-energy Fermi liquid form for each orbital: $\Sigma_m(\omega) = (1 - 1/Z_m)\omega - iA_m(\omega^2 + \pi^2 k_B^2 T^2)$ in the full expression (1). The calculated spectra deviate from the simple Drude fit above ∼3 meV in both channels. A better description of the data up to ∼20–30 meV is obtained using the generalized Drude fit, which on a log-log scale has the shape of two peaks of similar height separated by a dip. This dip signals the crossover from the regime in which the scattering rate is dominated by temperature to that in which it is dominated by its Fermi liquid frequency dependence [36,57]. It is apparent in the DFT+DMFT spectra around 25 meV and also (at a somewhat lower frequency) in the B_{1g} experimental spectra, as noted in Ref. [24].

In the B_{1g} channel, deviations between the calculated DFT+DMFT spectra and Fermi liquid behavior are apparent on Fig. 2(a). Weak deviations are first noticeable at frequencies of ∼20–30 meV, where the real-part of the self-energy (see Appendix B) deviates from the strict linear-in-ω Fermi liquid behavior (which also causes "kinks" observed in angular resolved photoemission experiments at similar frequencies [39,59,60]). As the frequency increases, the deviations become much more pronounced above $\hbar\omega \sim 100$ meV, where the DFT+Fermi liquid result starts to drop, while the full DMFT result continues to increase. The enhancement of the Raman response in this energy range is linked to a non-Fermi liquid feature of the DMFT self-energies Σ, which is a hallmark of Hund metal behavior. The real part $\mathrm{Re}\Sigma$ for both orbitals displays a minimum and an abrupt change of slope for $\hbar\omega \gtrsim 100$ meV [26] (see Appendix D), leading to an "unrenormalization" and waterfall in the quasiparticle dispersion. This feature that also causes a shoulder structure in the quasiparticle peak [35] has been shown to enhance the optical conductivity in this frequency range [36]. We note that in Ref. [36] the relation to Hund physics was missed. In Appendix D, we compare the results also to a calculation at increased occupancy $N = 5$, explicitly showing that the enhanced Raman response in the 100–500 meV range is due to the Hund metal inner structure of the quasiparticle peak. This effect is due to the two-stage coherence which is a hallmark of Hund metals: distinct coherence scales for spin and orbital degrees of freedom lead to additional structures in both one- and two-particle responses [27,33,61–63].

Figure 2 also displays the experimental data from Refs. [24,58]. Our analysis suggests that the observed increase of the experimental spectra, peaking at ∼400 meV, is a manifestation of the Hund metal non-Fermi liquid feature discussed above. Comparison to the DFT+Fermi liquid approximation demonstrates that this increase cannot be interpreted in terms of inter-band effects, which are fully taken into account in this approximation. Furthermore, in Refs. [24,58] it was shown that luminescence cannot account entirely for this increase. The clear signature of Hund metal behavior in Raman spectroscopy is the first main result of our work.

Figure 2(b) shows the results for the B_{2g} channel, along with the $A_{1g} + B_{2g}$ channel for which experimental data are available in a wider frequency range [58]. The results are similar to those in the B_{1g} channel and notably also display the non-Fermi liquid increase above 100 meV. In addition, the spectra display a clear "hump" around 80 meV. This hump is visible in $A_{1g} + B_{2g}$ and is even more pronounced in B_{2g} but does not appear in the B_{1g} channel. As the hump also appears in the DFT+Fermi liquid approximation, it cannot be attributed to non-Fermi liquid physics. Moreover, if one

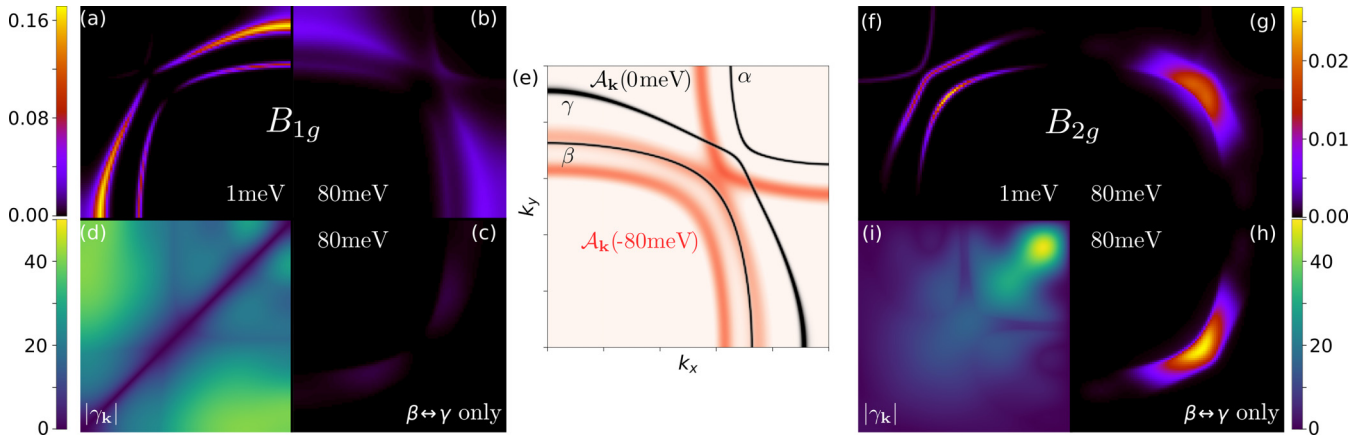

FIG. 3. Momentum-resolved Raman response. The (k_x, k_y) map of contributions to total $\chi''_{B_{1g}}$ at $\Omega = 1$ meV (a) and at $\Omega = 80$ meV (b). (c) The interband ($\beta \leftrightarrow \gamma$) contributions at $\Omega = 80$ meV. (d) The magnitude of the Raman vertex $|\gamma^{B_{1g}}| = \sum_\nu |\gamma^{B_{1g}}_{\nu\nu}|$. Panel (e) depicts the spectral function at two energies. In (f)–(h) the same information as in (a)–(d) is shown but for the B_{2g} channel. The response and vertex values are all in atomic units.

isolates the response corresponding to either of the two orbitals individually, one does not find a hump at that frequency (see Appendix C). Instead, we find the hump is a consequence of unexpectedly strong interband transitions.

We demonstrate this on Fig. 4, where we plot the full DFT+DMFT results next to a calculation that retains only the interband contributions to the response. We observe that whereas in B_{1g} the interband terms represent a small part of the full response, their contribution becomes dominant in B_{2g} around 80 meV. Additionally, we observe that at low energies, the data in B_{1g} and B_{2g} behave similarly. This raises the question of identifying which orbitals are probed by each channel and whether a particular channel acts as an orbital filter. The remainder of the paper discusses this point and explains why the interband contribution at 80 meV is so strong.

In Figs. 3(a) and 3(f), we present a map of the contribution of different momenta to χ'', i.e., of the momentum-resolved Raman response corresponding to the integrand in Eq. (1), at a low frequency (1 meV) for the B_{1g} and B_{2g} cases, respectively. This map exhibits the expected symmetry with maxima along the zone verticals/horizontals for B_{1g} and along the zone diagonals for B_{2g}. This is caused by the momentum dependence of the corresponding vertices—see Figs. 3(d) and 3(i) depicting their magnitude. On Figs. 3(a) and 3(f), one can distinguish the individual Fermi surface sheets and see that dominantly γ and β sheets contribute to both responses and that the B_{1g} response is primarily associated with the γ sheet, which is composed primarily of the xy orbital along the directions [39], where the B_{1g} vertex is large (see also Appendix E for discussion of orbital character of different channels). More precisely, the weights of the B_{1g} signal on sheets α, β, γ are, respectively, 0%, 16%, and 84%, while they are are 5%, 44%, and 51%, respectively, for the B_{2g} signal. The α sheet contributes minimally to both responses due to the low magnitude of the vertices in the corresponding part of the Brillouin zone. From this analysis, it is clear that the B_{1g} response is dominated by the xy orbital (with some smaller contribution from xz/yz), while in contrast the B_{2g} channel does not filter out a specific orbital contribution.

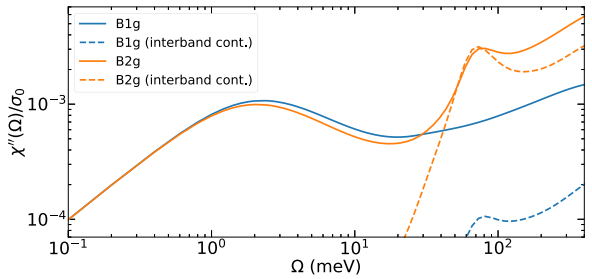

FIG. 4. Normalized Raman response for B_{1g} (blue) and B_{2g} (orange) at 29 K. The dashed lines indicate the interband contributions (see Appendix F).

Figures 3(b) and 3(g) depict the Raman response at 80 meV. In the B_{1g} channel, the momentum map is essentially a broadened version of the low-frequency case and one can still resolve the individual sheets. Conversely, in the B_{2g} channel, the momentum structure changes, revealing a strong broad feature appearing between the β and γ sheets. Figures 3(c) and 3(h) again present a map of the response at 80 meV but retaining only the contributions that involve interband β-γ transitions. This clearly shows that the B_{2g} signal in Fig. 3(g) is dominated by those transitions, whereas for B_{1g} in Fig. 3(c) their contribution is weak.

Why do the interband transitions become important only around 80 meV? Figure 3(e) shows an overlay of the momentum resolved spectral function evaluated at $\omega = 0$ (black, corresponding to the Fermi surface) and at $\omega = -80$ meV (red, corresponding to the renormalized equal-energy surface for quasiparticles at that binding energy). It is evident that the two spectral functions nearly completely nest, leading to strong interband effects whenever the vertex allows for such transitions. This motivates us to return to revisit the B_{1g} case in Fig. 3(c). We find that actually the interband contributions are of comparable magnitude in the two-channels (notice the different scales), but in the B_{1g} the magnitude of the intraband transitions is higher, resulting in less prominent interband contributions in the B_{1g} response (see also Appendix F).

The interband transitions also affect interpretation of the extended Drude modeling of the data. In Appendix A we demonstrate that consistently with Ref. [24] we find larger mass enhancements in B_{2g} channel, but we stress their large magnitude is due to the interband-transitions.

IV. CONCLUSIONS

In summary, we used a material-realistic DMFT approach with Raman vertices evaluated in a matrix-valued effective mass approximation to calculate the Raman response in Sr_2RuO_4. We documented the Fermi liquid regime at low energy and argued that the enhanced response at higher energies is a consequence of the inner structure of quasiparticle peak, a characteristic fingerprint of Hund metals. We found that the B_{2g} response is strongly influenced by interband contributions that are enhanced by a finite-frequency nesting effect. Whether this effect leads to a possible feedback of the corresponding fluctuations into other physical properties and is visible in other spectroscopies [64] are interesting questions for future investigations. Our results emphasize that this rarely discussed effect [65] is to be considered in other materials as well. On the methodology side, our investigation highlights the importance of material-realistic calculations of the Raman response and the approach developed in this work opens up possibilities for investigations of other materials with strong electronic correlations.

ACKNOWLEDGMENTS

We thank Yann Gallais and Jean-Côme Philippe for very useful discussions and for sharing their raw data and also acknowledge discussions with A. Tamai, F. Baumberger, and A. Hunter. G.B. and J.M. are supported by Slovenian Research Agency (ARRS) under Grants No. P1-0044 and No. J1-2458. The Flatiron Institute is a division of the Simons Foundation. The authors gratefully acknowledge the HPC RIVR consortium (www.hpc-rivr.si) and EuroHPC JU (eurohpc-ju.europa.eu) for funding this research by providing computing resources of the HPC system Vega at the Institute of Information Science (www.izum.si).

APPENDIX A: GENERALIZED DRUDE DESCRIPTION

1. Raman susceptibility

Raman susceptibility can be discussed in terms of the generalized Drude model, analogously to the more familiar optical conductivity. One can define the Raman conductivity $\sigma(\Omega) = \sigma'(\Omega) + i\sigma''(\Omega)$ with σ', σ'' denoting real and imaginary parts. The Raman conductivity is related to the Raman susceptibility by the relation $\sigma'(\Omega) = \chi''(\Omega)/\Omega$ [66]. As for the optical conductivity, one can express the Raman conductivity in a form similar to the Drude expression ("generalized Drude model"; see, e.g., Ref. [57])

$$\sigma(\Omega) = \chi_0 \frac{\mathcal{D}(\Omega)}{-i\Omega + \mathcal{D}(\Omega)\Gamma^*(\Omega)}, \tag{A1}$$

where

$$\chi_0 = \frac{2}{\pi}\int_0^{\Omega_c} \sigma_1(\Omega) d\Omega, \tag{A2}$$

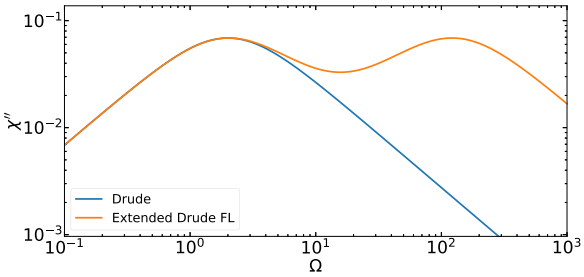

FIG. 5. Raman susceptibility in the extended Drude model with Fermi liquid $\Gamma^* \propto (\omega^2 + (2\pi k_B T)^2)$ and low energy Drude behavior Γ^* =const (blue).

The cutoff Ω_c can be taken to be infinite, but later we will use a finite value. In this expression the renormalization factor

$$\mathcal{D}(\Omega) = \frac{1}{1+\lambda(\Omega)} = \frac{m}{m^*(\omega)} \tag{A3}$$

is the inverse of the Raman mass enhancement and $\Gamma^*(\Omega)$ the Raman scattering rate. At low energies, $\mathcal{D}$ tends to a constant and one can write

$$\sigma(\Omega) \approx \frac{\chi_0^*}{-i\Omega + \Gamma^*(\Omega)}, \tag{A4}$$

where χ_0^* and Γ^* denote the renormalized Raman "plasma frequency" and the renormalized scattering rate.

Hence, the imaginary part of Raman susceptibility can be described with

$$\chi''_{\mathrm{EDM}}(\Omega) = \Omega\chi_0^* \frac{\Gamma^*(\Omega)}{\Omega^2 + [\Gamma^*(\Omega)]^2}. \tag{A5}$$

The Raman susceptibility corresponding to a Drude behavior $\Gamma^* \to$ const and to the Fermi liquid behavior $\Gamma^* \to \alpha[\Omega^2 + (2\pi k_B T)^2]$ is shown in Fig. 5. Notice the occurrence of the intermediate Fermi liquid minimum in the Fermi liquid case [24,56], and the associated two-hump shape, apparent on the log-log plot.

2. Low-energy behavior of Raman response in Sr_2RuO_4—the effective masses and scattering rates

In Ref. [24], such a generalized Drude analysis was applied to the experimental Raman spectra and the reported effective mass enhancement was found to be larger in the B_{2g} channel as compared to the B_{1g} one. We show here that the same conclusion applies to our theoretical results and explain why this is nonetheless consistent with our finding that the B_{1g} channel is dominated by the xy orbital/γ-sheet which is known to have the largest quasiparticle mass.

The mass-enhancement factor corresponding to the Raman response can be calculated from

$$1 + \lambda(\Omega) = \chi_0 \frac{\chi'(\Omega)}{|\chi(\Omega)|^2}. \tag{A6}$$

Figure 6(a) presents the behavior of χ_0 as a function of T. Similarly to what is found in measurements of Ref. [24] χ_0 in the B_{1g} drops strongly with temperature, whereas the B_{2g} depends on T less (our results show a weak increase with T). Figure 6(b) shows the behavior of the mass enhancements. Weaker mass enhancement is found in the B_{1g}

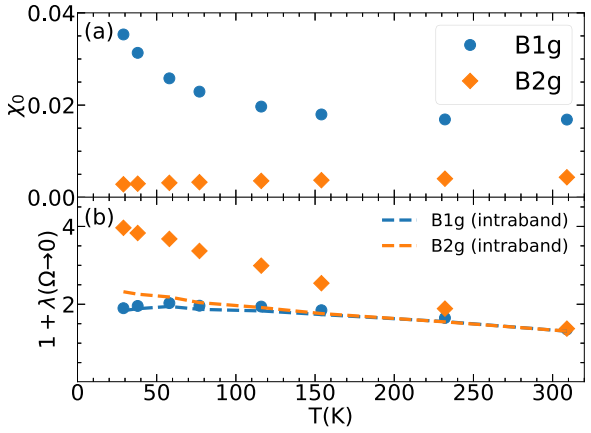

FIG. 6. (a) Temperature dependence of χ_0 in atomic units. (b) The mass-enhancement factor $(1+\lambda)$. In dotted line the mass-enhancement factor if only intraband contributions are considered. We used $\Omega_c = 500$ meV.

channel. Additionally, we show the result of a calculation in which we neglect the interband terms. This demonstrates that the stronger mass enhancements in B_{2g} are caused by the interband terms. In particular, the large interband contribution leads to an underestimation of relative weight of the low-energy response when applying a generalized Drude analysis, hence leading to an overestimation of the effective mass enhancement.

On Fig. 7 we plot the Raman scattering rate

$$\Gamma(\Omega) = \chi^0 \Omega \frac{\chi''(\Omega)}{|\chi(\Omega)|^2}, \tag{A7}$$

versus $\Omega^2 + (p\pi k_B T)^2$, to demonstrate the Fermi liquid behavior at low temperatures and energies. One sees the data obeys the Fermi liquid expectations with the Ghurzi factor $p = 2$ for the B_{1g} channel, but a smaller value $p = 1.5$ must be used for the B_{2g} channel.

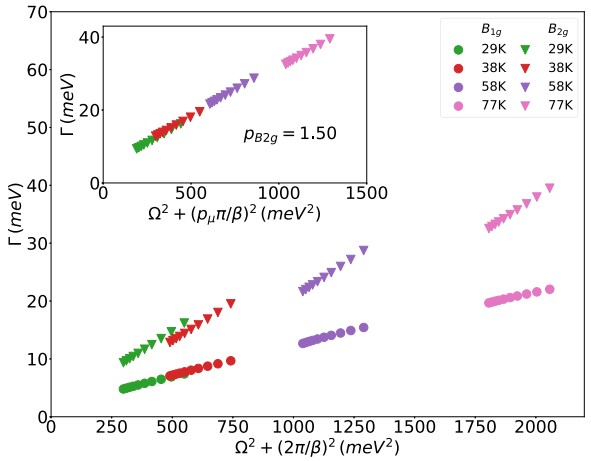

FIG. 7. Raman relaxation rate in B_{1g} and B_{2g} channels (circles and triangle, respectively) vs $(\Omega^2 + (p\pi k_B T)^2$. In main panel we use $p = 2$ and canonic Fermi liquid behavior is indicated by linear behavior. In B_{2g} the scattering rate is not linear in $[\Omega^2 + (p\pi k_B T)^2]$ for $p = 2$. Inset demonstrates the data collapse to a linear function when $p = 1.5$ is used instead.

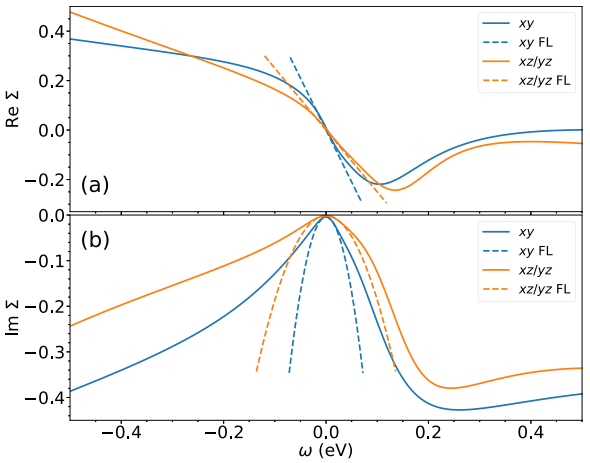

FIG. 8. Real (a) and imaginary (b) part of the self-energy for the orbital xy (blue) and xz/yz (orange) at 29 K. Fermi liquid low energy fits are indicated (dashed).

APPENDIX B: SELF-ENERGIES

The self-energies used in the calculations for temperature $T = 29$ K are shown in Fig. 8. The Fermi liquid (FL) linear-in-ω dependence in ReΣ and quadratic dependence in ImΣ $\propto (\omega^2 + \pi^2 k_B^2 T^2)$, are also indicated. Notice abrupt change of slope in ReΣ at $\omega = 0.1$ eV. This abrupt "unrenormalization" linked to Hund metal nature (Appendix D) leads to an enhancement of Raman response above this frequency.

APPENDIX C: INDIVIDUAL ORBITAL RESPONSE: ALLEN FORMULA

It is of interest to know the Raman response corresponding to individual orbitals. In an idealized case where there is no orbital-mixing and the band structure effects are weak (i.e., the energy dependence of the band transport function $\Phi(\epsilon) = \sum_{\mathbf{k}} \gamma_{\mathbf{k}}^2 \delta(\epsilon - \epsilon_k)$ is weak [57]) the Raman response is given by the Allen formula [67]

$$\chi''(\Omega) \propto \mathrm{Im} \int_{-\infty}^{\infty} d\omega \frac{f(\omega) - f(\omega + \Omega)}{\Omega + \Sigma^*(\omega) - \Sigma(\omega + \Omega)}. \tag{C1}$$

The Allen formula is expressed in terms of one component of self-energy alone and corresponds to an "ideal Raman filter."

In Fig. 9, we show the Allen formula results [normalized by $\sigma(0) = \chi''(\Omega)/\Omega|_{\Omega\to 0}$ so that the data match for small Ω] calculated with the DMFT self-energies for the two orbitals

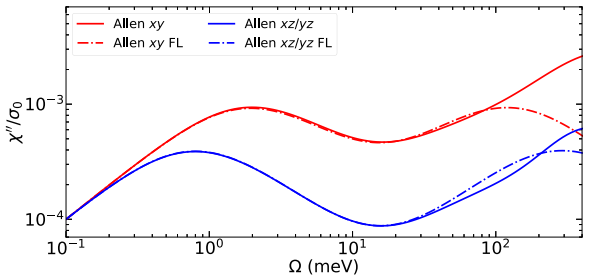

FIG. 9. Normalized Raman response using Allen formula Eq. (C1) for xy (red) and xz/yz orbital (blue). The results using corresponding Fermi liquid fits are also shown (dashed-dotted line).

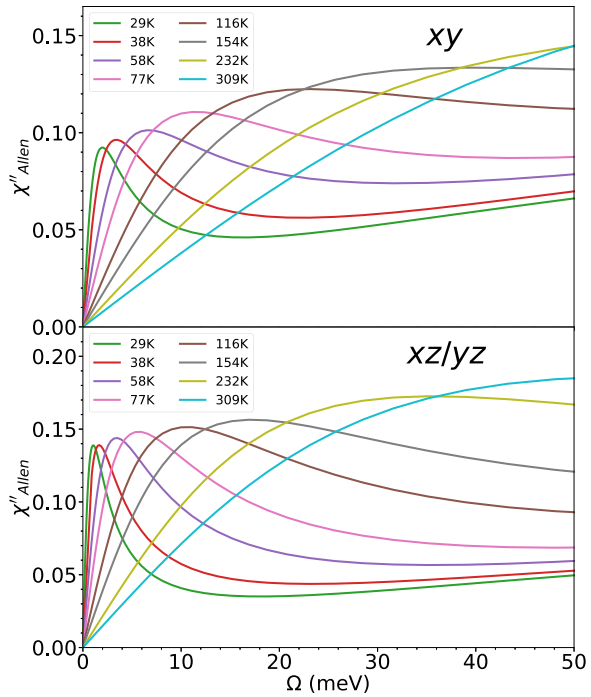

FIG. 10. Allen formula response for orbital xy (top) and xz/yz (bottom) for different temperatures. The Fermi liquid self-energy is $\Sigma_{\rm FL}(\omega) = (1 - 1/Z_m)\omega - iA_m(\omega^2 + \pi^2 k_B^2 T^2)$, where $Z_{xy} = 0.19$ and $A_{xy} = 66$, and $Z_{xz/yz} = 0.29$, $A_{xz/yz} = 18.5$. Same values were used in Fig. 2 of the main text.

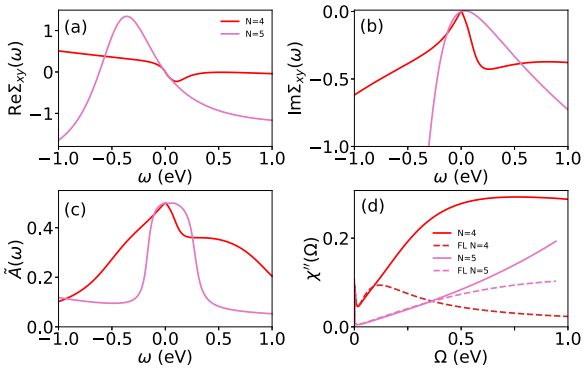

FIG. 11. Calculation with the self-energies obtained from DMFT for xy orbital and $\beta = 400$ for Sr_2RuO_4 in red ($N = 4$), and using the same band-structure but considering increased occupancy $N = 5$ in pink. The real and imaginary part of the self-energy are compared in panels (a) and (b), respectively. In panel (c) the corresponding proxy-spectral functions $\tilde{A}$ are compared. In panel (d) the corresponding Raman response $\chi''(\Omega)$ obtained from Allen formula (full) are shown and the results are additionally compared to the response of the corresponding Fermi liquid (dashed lines).

(full) and compare the results also to what one obtains using a Fermi liquid fit to the two self-energies (dashed-dotted). In xz orbital one sees a narrower Drude-peak followed by a more pronounced Fermi liquid intermediate minimum than what one sees for xy. This is consistent with a more coherent response in the xz orbital known from earlier work [26,36]. Except for the small deviations at 30 meV, FL describes the behavior pretty well all the way up to 100 meV for the xy and 200 meV for the xz orbital. Because these results correspond to an "ideal Raman filter" that would selectively probe each of the two orbitals, and because the 80 meV hump feature discussed in the main text is not observed in either of the two, its occurrence cannot be explained in terms of the orbital-physics/correlations. At higher frequencies the actual response strongly exceeds the Fermi liquid response, which is a signature of Hund metals as discussed next.

In Fig. 10 we present the Allen formula results for several temperatures for xy (top) and xz (bottom) orbitals. With the exception of a broader Drude peak found for the xy case, the two sets of data behave similarly.

APPENDIX D: HUND METAL SIGNATURE

In this section, we relate the enhancement seen in the Raman response at frequencies above 0.1 eV to the shape of single particle density of states that we argue is characteristic of Hund metals. To demonstrate this we also performed calculations using Sr_2RuO_4 band structure but at increased occupancy of $N = 5$ electrons in t_{2g} orbitals, which provides a reference where no Hund metal effects are present. In those calculations we increased the Hubbard interaction parameter to $U = 4.2$ eV so that the resulting mass enhancement is the same as that of the $N = 4$ calculation.

On Fig. 11(a) we show $\mathrm{Re}\Sigma(\omega)$ for xy orbital at 29 K. In Hund metal case (red) the strong deviation from low-energy linear behavior in $\mathrm{Re}\Sigma$ occurs at a low energy 0.1 eV. Conversely in the $N = 5$ result (pink) deviations occur at larger energies only.

To see how these differences affect the spectral function it is convenient to consider a proxy quantity $\tilde{A}(\omega)$

$$\tilde{A}(\omega) = -(1/\pi)\mathrm{Im}\int d\varepsilon\, \tilde{\rho}(\varepsilon)[\omega - \varepsilon - \Sigma(\omega)]^{-1} \qquad \text{(D1)}$$

that gives the density of states of an auxiliary reference single-orbital problem. For this auxiliary problem we take a flat noninteracting DOS with $\tilde{\rho}(\varepsilon)$ being a nonzero constant in the range $[-1\,\mathrm{eV}, 1\,\mathrm{eV}]$ and vanishing elsewhere. Using such featureless DOS is convenient to assure that all features in $\tilde{A}$ are caused by correlation effects. The results are shown in Fig. 11(c). The $N = 5$ calculation has a shape that is characteristic of standard correlated metals with a narrow quasiparticle peak with a shape resembling narrowed bare DOS whereas $N = 4$ calculation displays a richer structure characteristic of Hund metals with slow decrease of the spectral function at negative energies and a side-hump feature at positive energies.

We use the Allen formula [Eq. (C1)] and calculate also the corresponding response χ''. In Fig. 11(d) we compare the results also against the Fermi liquid fits [distinct for the $N = 4$ and $N = 5$ calculation because the curvatures of the fitted imaginary parts of self-energies are distinct as seen in Fig. 11(b)]. The Fermi liquid behavior is followed to much larger frequencies for the $N = 5$ calculation and the deviations from the Fermi liquid are much smaller than that seen in the $N = 4$ calculation, which demonstrates that strong increase of Raman response in the 0.1–0.5 eV range discussed in the main text is a signature of the Hund metal.

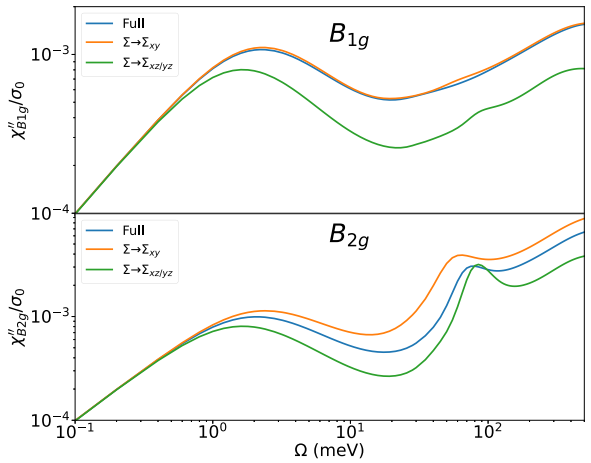

FIG. 12. Raman response for B_{1g} (top) and B_{2g} (bottom) channels for 29 K. The calculation using the self-energy of the Sr_2RuO_4 (blue line) is compared to the case where the self-energy for all orbitals is given by that corresponding to the orbital xy (orange) or the orbital xz/yz (green).

APPENDIX E: RAMAN RESPONSE FOR TRIAL SELF-ENERGIES

To disentangle different physical effects that contribute to the calculated Raman response it is convenient to perform calculations evaluating the Raman response with Eq. (1) from the main text, but substituting the self-energies with different trial values $\Sigma \to \Sigma_{\text{trial}}$. In Fig. 12 we compare the full Raman response (blue line) with that of a trial calculation where all orbital components of the self-energy were set to that of the xy orbital (orange line) and to the xz/yz orbital (green line). For the B_{1g} (top panel) we observe matching between orange and blue lines, indicating that B_{1g} is mainly contributed by the states involving the xy orbital. Conversely, in B_{2g} the full result is in the middle of the two-trial calculations, suggesting both xz/yz and xy orbitals contribute similarly to the response.

APPENDIX F: INTERBAND CONTRIBUTIONS

In Eq. (1) in the main text, the response has intra-band, inter-band, and mixed contributions. Namely, both spectral functions and Raman vertices have interband components. The spectral density in the band basis is $\mathcal{A}_k = (\omega + \mu - \epsilon_k + \Sigma^{\text{band}})^{-1}$ where $\Sigma^{\text{band}} = P\Sigma^{\text{orb}}(\omega)P^\dagger$. Σ^{band} and Σ^{orb} are the self-energy in the band basis and orbital basis respectively and P is the transformation matrix between the two basis. It is convenient to ne $\mathcal{A}_k$ is diagonal in band basis (this is strictly correct in the case of $\Sigma^{\text{orb}} \propto \mathbb{I}$). Under this assumption, the Raman response separates into terms that come from the diagonal terms of the vertex $\gamma^\mu_{\mathbf{k}}$ (the intraband terms) and from the off-diagonal terms (the interband contributions). Namely,

$$\text{Tr}\,\gamma^\mu_{\mathbf{k}}\,\mathcal{A}_{\mathbf{k}}(\omega)\,\gamma^\mu_{\mathbf{k}}\,\mathcal{A}_{\mathbf{k}}(\omega+\Omega) \to \begin{cases} \text{intraband}: & \sum_\nu \gamma^\mu_{\nu\nu}\,\mathcal{A}_{\nu\nu}(\omega+\Omega)\,\gamma^\mu_{\nu\nu}\,\mathcal{A}_{\nu\nu}(\omega) \\ \text{interband}: & \sum_{\nu\neq\tau} \gamma^\mu_{\nu\tau}\,\mathcal{A}_{\tau\tau}(\omega+\Omega)\,\gamma^\mu_{\tau\nu}\,\mathcal{A}_{\nu\nu}(\omega) \end{cases}. \tag{F1}$$

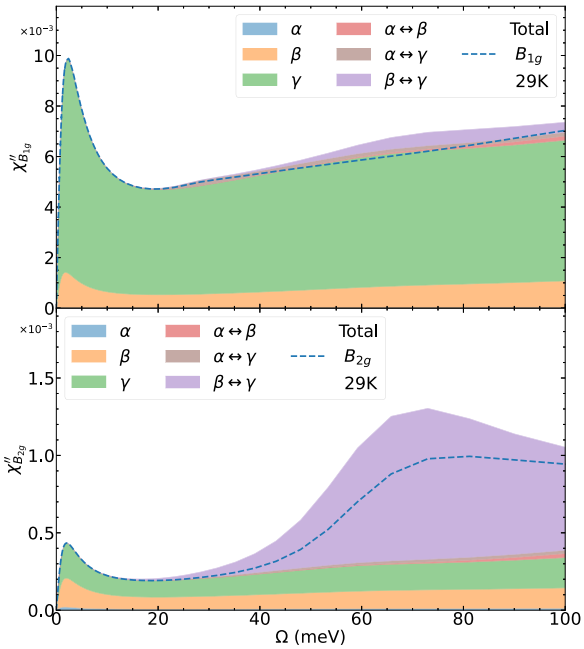

FIG. 13. Contributions to the Raman response for the B_{1g} channel (top) and B_{2g} channel (bottom) at 29 K presented in terms of additive contributions (shading) in atomic units.

Such decomposition is used to analyze the intraband and interband contributions to Raman susceptibility presented in the form of stacked area chart on Fig. 13. Different intraband contributions (blue, orange, and green shading for, respectively, α, β, γ bands) and interband contributions (red, brown, violet) are indicated. One sees that for B_{1g} channel, the majority of the response comes from intraband terms and in particular the γ band. Conversely, for B_{2g} above 30 meV the interband $\beta \leftrightarrow \gamma$ transitions start dominating. Notice that the interband transitions are maximal close to 75 meV in both channels and that their absolute magnitude is actually comparable in the two channels. The qualitative distinction in the behavior between the two channels comes from the fact that the intraband terms are much smaller in B_{2g}, which in turn is due to the fact that the nearest neighbor hoppings do not contribute in that channel. Note also that the sum of the contributions exceeds somewhat the total Raman response (blue dashed line), which is due to the neglected off-diagonal parts of the spectral functions in the band basis in this analysis. Namely, if one retains those, then there are additional mixed contributions to the response which are of the form

$$\begin{aligned} \text{mixed 1}: & \sum_{\nu\neq\tau} \gamma^\mu_{\nu\nu}\,\mathcal{A}_{\nu\tau}(\omega+\Omega)\,\gamma^\mu_{\tau\tau}\,\mathcal{A}_{\tau\nu}(\omega) \\ \text{mixed 2}: & \sum_{\nu\neq\tau} \gamma^\mu_{\nu\tau}\,\mathcal{A}_{\tau\tau}(\omega+\Omega)\,\gamma^\mu_{\tau\tau}\,\mathcal{A}_{\tau\nu}(\omega) \\ \text{mixed 3}: & \sum_{\nu\neq\nu'\neq\tau\neq\tau'} \gamma^\mu_{\nu\nu'}\,\mathcal{A}_{\nu'\tau}(\omega+\Omega)\,\gamma^\mu_{\tau\tau'}\,\mathcal{A}_{\tau'\nu}(\omega) \end{aligned} \tag{F2}$$

and give a negative contribution to the response.

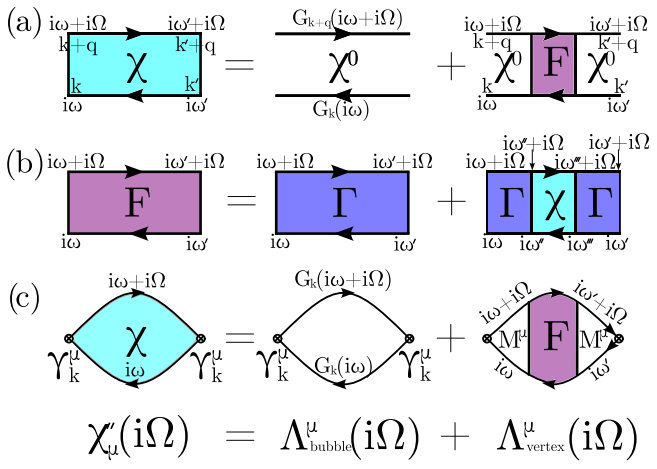

FIG. 14. Diagrammatic representation of the many-body vertex corrections to the Raman response. (a) Vertex corrections to the lattice particle-hole susceptibility χ. (b) Reducible vertex F expressed in terms of the irreducible vertex Γ. (c) Full Raman responses (or optical conductivity, if the Raman vertex is substituted by that of velocity $\gamma \to v$). We denote $M = G\gamma G$. Summation over momentum k and Fermionic frequencies ω are implied.

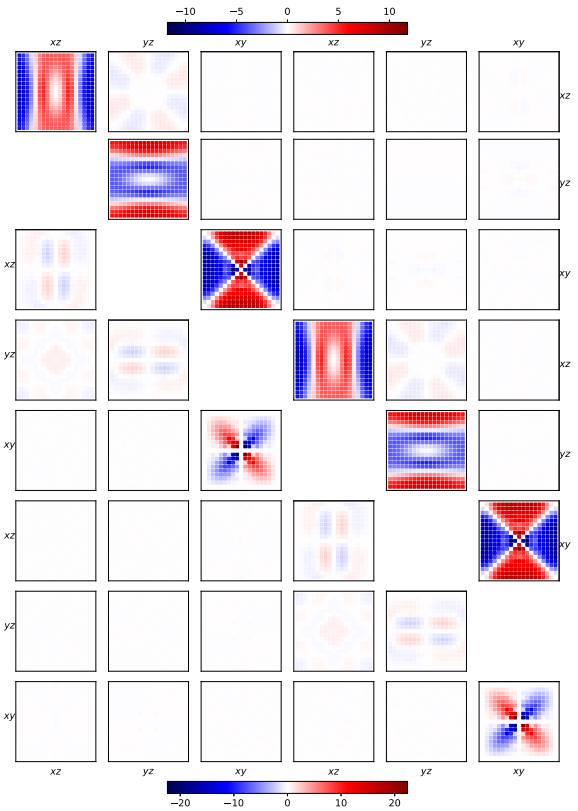

FIG. 15. Value of the Raman vertex in a plane $k_z = 0$. Each orbital index combination m, m' (for the six spin-orbitals) is shown in a separate panel. The scale is kept the same within the same channel for better comparison. The panels in the upper triangle correspond to the B_{1g} channel, and the one in the lower triangle to the B_{2g} channel. The values are in atomic units.

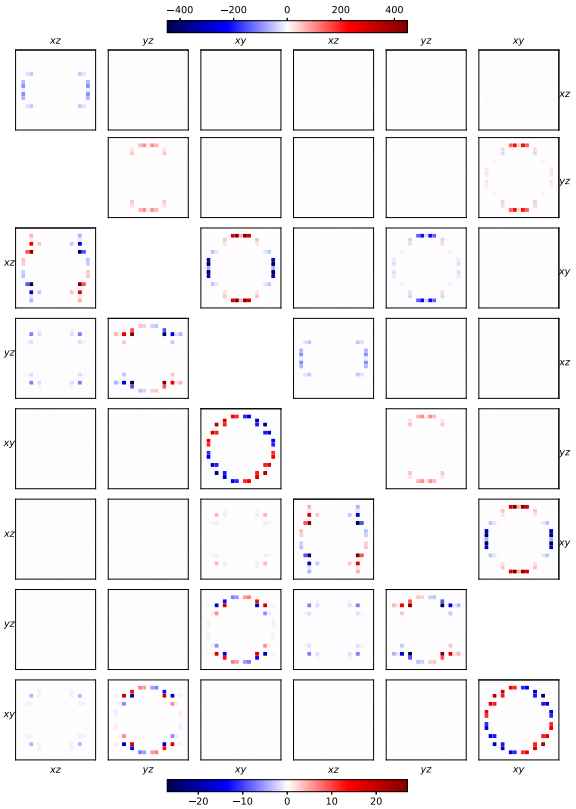

FIG. 16. Value of $\sum_{m,m'} \gamma_{\mathbf{k}mm'} A_{\mathbf{k}m'm''}(\omega = 0) A_{\mathbf{k}m'''m}(\omega = 0)$ in a plane $k_z = 0$. Each orbital index combination m'', m''' (for the six spin-orbitals) is shown in a separate panel. The scale is kept the same within the same channel for better comparison. The panels in the upper triangle correspond to the B_{1g} channel, and the one in the lower triangle to the B_{2g} channel. The values are in atomic units.

APPENDIX G: EXPRESSION FOR A_{1g}+B_{2g} VERTEX

A_{1g}+B_{2g} is probed by both incident and reflected light being polarized inplane at 45 degrees to the nearest neighbor Ru-O bond, i.e., in 110 direction (using conventional unit cell notation). The corresponding vertex reads

$$\gamma_{\mathbf{k}}^{A_{1g}+B_{2g}} = \frac{\partial^2 H^{(W)}}{\partial k_x \partial k_y} + \frac{1}{2}\left(\frac{\partial^2 H^{(W)}}{\partial k_x^2} + \frac{\partial^2 H^{(W)}}{\partial k_y^2}\right). \tag{G1}$$

APPENDIX H: VERTEX CORRECTIONS

It is well known that for inversion-symmetric systems the vertex corrections (VCs) to optical conductivity in DMFT vanish [13,51]. This is because in DMFT, the many-body vertex (i.e., the object F depicted in diagrams shown in Fig. 14, not to be confused with the Raman vertex γ) is local and VCs are then given by terms of the form $\sum_{\mathbf{k}} v_{\mathbf{k}} G_{\mathbf{k}} G_{\mathbf{k}}$ which vanish by symmetry (namely, velocity $v_{\mathbf{k}}$ is odd under $\mathbf{k} \to -\mathbf{k}$, whereas the Green's function $G_{\mathbf{k}}$ is even). The situation in multiband problems is more subtle, but one can argue that under some limitations the vertex correction vanish there, too [68]. We checked that in Sr_2RuO_4, the Green's function matrix (in orbital basis) has even parity and velocity matrix is odd under inversion, so the argument applies and the VCs to optical conductivity in DMFT vanish.

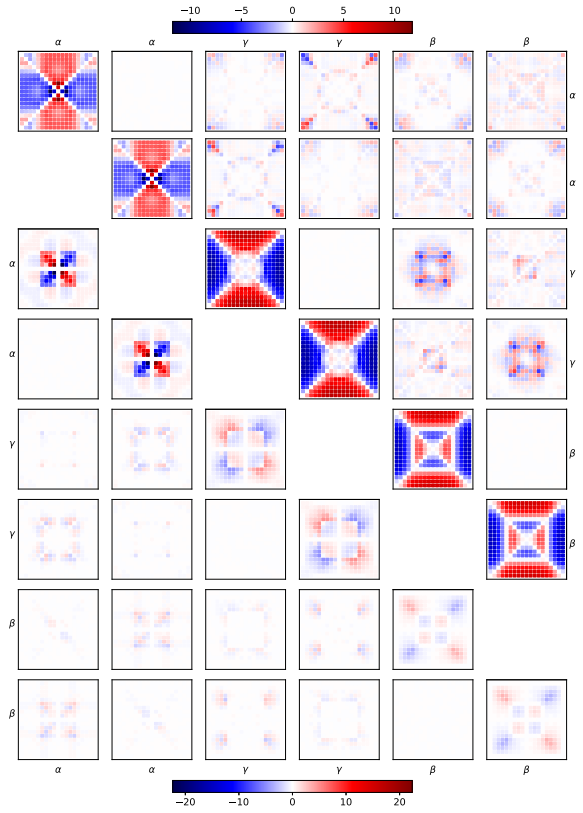

FIG. 17. Value of the Raman vertex in a plane $k_z = 0$. Each band index combination ν', ν' (for the six spin-orbital bands) is shown in a separate panel. The scale is kept the same within the same channel for better comparison. The panels in the upper triangle correspond to the B_{1g} channel, and the one in the lower triangle to the B_{2g} channel. The values are in atomic units.

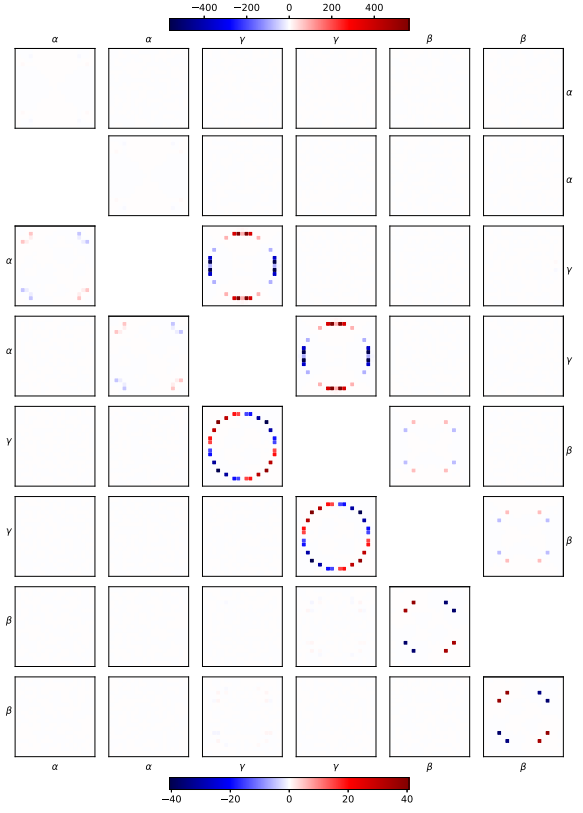

FIG. 18. Value of $\sum_{\nu,\nu'} \gamma_{\mathbf{k}\nu\nu'} A_{\mathbf{k}\nu'\nu''}(\omega = 0) A_{\mathbf{k}\nu'''\nu}(\omega = 0)$ in a plane $k_z = 0$. Each band index combination ν'', ν''' (for the six spin-orbital bands) is shown in a separate panel. The scale is kept the same within the same channel for better comparison. The panels in the upper triangle correspond to the B_{1g} channel, and the one in the lower triangle to the B_{2g} channel. The values are in atomic units.

What about Raman response? In cluster extensions of DMFT the VCs were shown to be relevant [18,69,70], but the situation in pure DMFT was to our knowledge not discussed before.

In the Raman response, the role of velocity is taken by Raman vertex $\gamma_{\mathbf{k}}$, which is not odd under inversion. However, other symmetries could also cause vanishing of $\sum_{\mathbf{k}} v_{\mathbf{k}} G_{\mathbf{k}} G_{\mathbf{k}}$. Consider a tight-binding model in 2D with the band energy $\varepsilon(k_x, k_y) = t[\cos(k_x) + \cos(k_y)] + t' \cos(k_x)\cos(k_y)$, with t, t' respectively the nearest neighbor hopping (next nearest neighbor hopping). For such a band, the Raman vertex in B_{1g} is $\gamma^{B_{1g}} = 1/2(\partial^2\varepsilon/\partial k_x^2 - \partial^2\varepsilon/\partial k_y^2) = t'[\cos(k_y) - \cos(k_x)]/2$ which is odd under reflections across zone diagonals $k_x = \pm k_y$, whereas the Green's functions are even under those reflections. Hence $\sum_{\mathbf{k}} \gamma_{\mathbf{k}}^{B_{1g}} G_{\mathbf{k}} G_{\mathbf{k}}$ vanishes. A similar argument applies to the B_{2g} channel, where $\gamma^{B_{2g}} = \partial^2\varepsilon/\partial k_x \partial k_y = t' \sin(k_x)\sin(k_y)$ and is odd under reflection across $k_x = 0$ and $k_y = 0$ planes.

What about the multiorbital Sr_2RuO_4 case? The momentum dependencies of the Raman vertex for different spin-orbital index combinations are shown in Fig. 15. Whereas these matrix elements do reflect symmetries, the momentum sum of $A_k \gamma_k A_k$ (shown in Fig. 16) does not vanish for all spin-orbital channels, so one cannot argue about the vanishing of VCs from those considerations alone. The momentum dependencies of the Raman vertex for each band index combination and the momentum sum of $A_k \gamma_k A_k$ are shown in Figs. 17 and 18, respectively.

Therefore, we evaluated the many-body vertex and calculated the corresponding VCs to the Raman response. The particle-hole reducible vertex F affects the propagation of particles and holes in the system following the Bethe-Salpeter equation for the particle-hole susceptibility $\chi = \chi^0 + \chi^0 F \chi^0$ where the summations over internal spin, orbital and Matsubara indices are implicit, diagrammatically depicted in Fig. 14(a). The fully reducible many-body vertex can itself be expressed in terms of the irreducible vertex Γ as $F = \Gamma + \Gamma\chi\Gamma$, depicted in Fig. 14(b). The full Raman response can then be separated as the sum of the bubble contributions Λ_{bubble} and the VCs Λ_{vertex}, depicted in Fig. 14.

We computed the many-body vertex $\Gamma \to \Gamma(i\omega_1, i\omega_2, i\Omega)$ from the impurity Bethe-Salpeter equation (where we obtained the full matrix two-particle Green's function using w2Dynamics [71]). $\chi \to \sum_{k,q} \chi(k, q; i\omega_1, i\omega_2, i\Omega)$ was obtained from the solution of lattice Bethe-Salpeter equation $\chi = \chi^0 + \chi^0\Gamma\chi$ as implemented in TPRF package of TRIQS [47,72,73]. We perform the sum over momentum points directly on the susceptibility because the many-body vertex is local in DMFT. Note that we neglected spin-orbit coupling in the construction of these objects.

We evaluated F on Matsubara axis at $\beta = 1/(k_B T) = 40/\text{eV}$, retaining 30 internal Matsubara frequencies and up to $16 \times 16 \times 16$ momentum points. We checked that F correctly describes the suppression of the uniform charge susceptibility from the results obtained by considering only the bubble diagram (2.4/eV) to that obtained considering the full susceptibility (1.4/eV), which we extracted from self-consistent calculations in a uniform field.

The VCs to the Raman response for the μ channel are then given by connected part of the Raman correlation function

$$\Lambda^{\mu}_{\text{vertex}}(i\Omega_n) \equiv M^{\mu}(i\Omega_n) F(i\Omega_n) M^{\mu}(i\Omega_n), \tag{H1}$$

where the sums over the Fermionic Matsubara frequencies are implicit and

$$M^{\mu}(i\omega_1, i\omega_2, i\Omega) \equiv \beta \sum_k G_k(i\omega_1)\gamma^{\mu}_k G_k(i\omega_2 + i\Omega)\delta_{\omega_1\omega_2}, \tag{H2}$$

with γ^{μ}_k the Raman vertex in the μ channel. We find the connected part to be significantly smaller than the bubble contribution. The ratio $r^{\mu} = \Lambda^{\mu}_{\text{vertex}}(i\Omega_n = 0)/\Lambda^{\mu}_{\text{bubble}}(i\Omega_n = 0)$ is below 1% for $\mu = \text{B}_{1g}$, and below 0.01% for $\mu = \text{B}_{2g}$.

[1] B. Schrader, (ed.), *Infrared and Raman Spectroscopy: Methods and Applications* (Wiley-VCH, Weinheim, Germany, 1995).

[2] T. P. Devereaux and R. Hackl, Inelastic light scattering from correlated electrons, Rev. Mod. Phys. **79**, 175 (2007).

[3] M. L. Tacon, A. Sacuto, A. Georges, G. Kotliar, Y. Gallais, D. Colson, and A. Forget, Two energy scales and two distinct quasiparticle dynamics in the superconducting state of underdoped cuprates, Nat. Phys. **2**, 537 (2006).

[4] A. Sacuto, Y. Gallais, M. Cazayous, S. Blanc, M.-A. Méasson, J. Wen, Z. Xu, G. Gu, and D. Colson, Electronic Raman scattering in copper oxide superconductors: Understanding the phase diagram, C. R. Phys. **12**, 480 (2011).

[5] B. Loret, N. Auvray, Y. Gallais, M. Cazayous, A. Forget, D. Colson, M.-H. Julien, I. Paul, M. Civelli, and A. Sacuto, Intimate link between charge density wave, pseudogap, and superconducting energy scales in cuprates, Nat. Phys. **15**, 771 (2019).

[6] F. Kretzschmar, T. Böhm, U. Karahasanović, B. Muschler, A. Baum, D. Jost, J. Schmalian, S. Caprara, M. Grilli, C. D. Castro, J. G. Analytis, J.-H. Chu, I. R. Fisher, and R. Hackl, Critical spin fluctuations and the origin of nematic order in $Ba(Fe_{1-x}Co_x)_2As_2$, Nat. Phys. **12**, 560 (2016).

[7] Y. Gallais and I. Paul, Charge nematicity and electronic Raman scattering in iron-based superconductors, C. R. Phys. **17**, 113 (2016).

[8] Y. Yao, R. Willa, T. Lacmann, S.-M. Souliou, M. Frachet, K. Willa, M. Merz, F. Weber, C. Meingast, R. Heid, A.-A. Haghighirad, J. Schmalian, and M. L. Tacon, An electronic nematic liquid in $BaNi_2As_2$, Nat. Commun. **13**, 4535 (2022).

[9] K. Sen, D. Fuchs, R. Heid, K. Kleindienst, K. Wolff, J. Schmalian, and M. L. Tacon, Strange semimetal dynamics in $SrIrO_3$, Nat. Commun. **11**, 4270 (2020).

[10] D. Jost, L. Peis, G. He, A. Baum, S. Geprägs, J. C. Palmstrom, M. S. Ikeda, I. R. Fisher, T. Wolf, S. Lederer, S. A. Kivelson, and R. Hackl, Quantum critical fluctuations in an Fe-based superconductor, Commun. Phys. **5**, 201 (2022).

[11] S. Maiti, A. V. Chubukov, and P. J. Hirschfeld, Conservation laws, vertex corrections, and screening in Raman spectroscopy, Phys. Rev. B **96**, 014503 (2017).

[12] M. Udina, M. Grilli, L. Benfatto, and A. V. Chubukov, Raman response in the nematic phase of FeSe, Phys. Rev. Lett. **124**, 197602 (2020).

[13] A. Georges, G. Kotliar, W. Krauth, and M. J. Rozenberg, Dynamical mean-field theory of strongly correlated Fermion systems and the limit of infinite dimensions, Rev. Mod. Phys. **68**, 13 (1996).

[14] J. K. Freericks, T. P. Devereaux, R. Bulla, and T. Pruschke, Nonresonant inelastic light scattering in the Hubbard model, Phys. Rev. B **67**, 155102 (2003).

[15] A. M. Shvaika, O. Vorobyov, J. K. Freericks, and T. P. Devereaux, Resonant enhancement of inelastic light scattering in strongly correlated materials, Phys. Rev. Lett. **93**, 137402 (2004).

[16] A. M. Shvaika, O. Vorobyov, J. K. Freericks, and T. P. Devereaux, Electronic Raman scattering in correlated materials: A treatment of nonresonant, mixed, and resonant scattering using dynamical mean-field theory, Phys. Rev. B **71**, 045120 (2005).

[17] L. de'Medici, A. Georges, and G. Kotliar, Sum-rules for Raman scattering off strongly correlated electron systems, Phys. Rev. B **77**, 245128 (2008).

[18] N. Lin, E. Gull, and A. J. Millis, Two-particle response in cluster dynamical mean-field theory: Formalism and application to the Raman response of high-temperature superconductors, Phys. Rev. Lett. **109**, 106401 (2012).

[19] T. Liu, D. Jost, B. Moritz, E. W. Huang, R. Hackl, and T. P. Devereaux, Tendencies of enhanced electronic nematicity in the Hubbard model and a comparison with Raman scattering on high-temperature superconductors, Phys. Rev. B **103**, 134502 (2021).

[20] S. Baroni, S. de Gironcoli, A. Dal Corso, and P. Giannozzi, Phonons and related crystal properties from density-functional perturbation theory, Rev. Mod. Phys. **73**, 515 (2001).

[21] M. Lazzeri and F. Mauri, First-principles calculation of vibrational Raman spectra in large systems: Signature of small rings in crystalline SiO_2, Phys. Rev. Lett. **90**, 036401 (2003).

[22] I. I. Mazin, T. P. Devereaux, J. G. Analytis, J.-H. Chu, I. R. Fisher, B. Muschler, and R. Hackl, Pinpointing gap minima in $Ba(Fe_{0.94}Co_{0.06})_2As_2$ via band-structure calculations and electronic Raman scattering, Phys. Rev. B **82**, 180502(R) (2010).

[23] B. Valenzuela, M. J. Calderón, G. León, and E. Bascones, Optical conductivity and Raman scattering of iron superconductors, Phys. Rev. B **87**, 075136 (2013).

[24] J.-C. Philippe, B. Baptiste, C. Sow, Y. Maeno, A. Forget, D. Colson, M. Cazayous, A. Sacuto, and Y. Gallais, Orbital dichotomy of Fermi liquid properties in Sr_2RuO_4 revealed by Raman spectroscopy, Phys. Rev. B **103**, 235147 (2021).

[25] A. P. Mackenzie and Y. Maeno, The superconductivity of Sr_2RuO_4 and the physics of spin-triplet pairing, Rev. Mod. Phys. **75**, 657 (2003).

[26] J. Mravlje, M. Aichhorn, T. Miyake, K. Haule, G. Kotliar, and A. Georges, Coherence-incoherence crossover and the mass-renormalization puzzles in Sr_2RuO_4, Phys. Rev. Lett. **106**, 096401 (2011).

[27] J. Mravlje and A. Georges, Thermopower and entropy: Lessons from Sr_2RuO_4, Phys. Rev. Lett. **117**, 036401 (2016).

[28] F. B. Kugler, M. Zingl, H. U. R. Strand, Seung-Sup B. Lee, J. von Delft, and A. Georges, Strongly correlated materials from a numerical renormalization group perspective: How the Fermi-liquid state of Sr_2RuO_4 emerges, Phys. Rev. Lett. **124**, 016401 (2020).

[29] Z. P. Yin, K. Haule, and G. Kotliar, Kinetic frustration and the nature of the magnetic and paramagnetic states in iron pnictides and iron chalcogenides, Nat. Mater. **10**, 932 (2011).

[30] A. Georges, L. de Medici, and J. Mravlje, Strong correlations from Hunds coupling, Annu. Rev. Condens. Matter Phys. **4**, 137 (2013).

[31] Z. P. Yin, K. Haule, and G. Kotliar, Fractional power-law behavior and its origin in iron-chalcogenide and ruthenate superconductors: Insights from first-principles calculations, Phys. Rev. B **86**, 195141 (2012).

[32] C. Aron and G. Kotliar, Analytic theory of Hund's metals: A renormalization group perspective, Phys. Rev. B **91**, 041110(R) (2015).

[33] K. M. Stadler, Z. P. Yin, J. von Delft, G. Kotliar, and A. Weichselbaum, Dynamical mean-field theory plus numerical renormalization-group study of spin-orbital separation in a three-band Hund metal, Phys. Rev. Lett. **115**, 136401 (2015).

[34] A. Horvat, R. Žitko, and J. Mravlje, Low-energy physics of three-orbital impurity model with Kanamori interaction, Phys. Rev. B **94**, 165140 (2016).

[35] H. Wadati, J. Mravlje, K. Yoshimatsu, H. Kumigashira, M. Oshima, T. Sugiyama, E. Ikenaga, A. Fujimori, A. Georges, A. Radetinac, K. S. Takahashi, M. Kawasaki, and Y. Tokura, Photoemission and DMFT study of electronic correlations in $SrMoO_3$: Effects of Hund's rule coupling and possible plasmonic sideband, Phys. Rev. B **90**, 205131 (2014).

[36] D. Stricker, J. Mravlje, C. Berthod, R. Fittipaldi, A. Vecchione, A. Georges, and D. van der Marel, Optical response of Sr_2RuO_4 reveals universal Fermi-liquid scaling and quasiparticles beyond Landau theory, Phys. Rev. Lett. **113**, 087404 (2014).

[37] F. B. Kugler, Seung-Sup B. Lee, A. Weichselbaum, G. Kotliar, and J. von Delft, Orbital differentiation in Hund metals, Phys. Rev. B **100**, 115159 (2019).

[38] G. Pizzi, V. Vitale, R. Arita, S. Blügel, F. Freimuth, G. Géranton, M. Gibertini, D. Gresch, C. Johnson, T. Koretsune, J. Ibañez-Azpiroz, H. Lee, J.-M. Lihm, D. Marchand, A. Marrazzo, Y. Mokrousov, J. I. Mustafa, Y. Nohara, Y. Nomura, L. Paulatto *et al.*, Wannier90 as a community code: New features and applications, J. Phys.: Condens. Matter **32**, 165902 (2020).

[39] A. Tamai, M. Zingl, E. Rozbicki, E. Cappelli, S. Riccò, A. de la Torre, S. McKeown Walker, F. Y. Bruno, P. D. C. King, W. Meevasana, M. Shi, M. Radović, N. C. Plumb, A. S. Gibbs, A. P. Mackenzie, C. Berthod, H. U. R. Strand, M. Kim, A. Georges, and F. Baumberger, High-resolution photoemission on Sr_2RuO_4 reveals correlation-enhanced effective spin-orbit coupling and dominantly local self-energies, Phys. Rev. X **9**, 021048 (2019).

[40] M. Kim, J. Mravlje, M. Ferrero, O. Parcollet, and A. Georges, Spin-orbit coupling and electronic correlations in Sr_2RuO_4, Phys. Rev. Lett. **120**, 126401 (2018).

[41] G. Zhang, E. Gorelov, E. Sarvestani, and E. Pavarini, Fermi surface of Sr_2RuO_4: Spin-orbit and anisotropic coulomb interaction effects, Phys. Rev. Lett. **116**, 106402 (2016).

[42] O. Parcollet, M. Ferrero, T. Ayral, H. Hafermann, I. Krivenko, L. Messio, and P. Seth, TRIQS: A toolbox for research on interacting quantum systems, Comput. Phys. Commun. **196**, 398 (2015).

[43] M. Aichhorn, L. Pourovskii, V. Vildosola, M. Ferrero, O. Parcollet, T. Miyake, A. Georges, and S. Biermann, Dynamical mean-field theory within an augmented plane-wave framework: Assessing electronic correlations in the iron pnictide LaFeAsO, Phys. Rev. B **80**, 085101 (2009).

[44] M. Aichhorn, L. Pourovskii, and A. Georges, Importance of electronic correlations for structural and magnetic properties of the iron pnictide superconductor LaFeAsO, Phys. Rev. B **84**, 054529 (2011).

[45] M. Aichhorn, L. Pourovskii, P. Seth, V. Vildosola, M. Zingl, O. E. Peil, X. Deng, J. Mravlje, G. J. Kraberger, C. Martins, M. Ferrero, and O. Parcollet, TRIQS/DFTTools: A TRIQS application for *ab initio* calculations of correlated materials, Comput. Phys. Commun. **204**, 200 (2016).

[46] D. Sutter, C. G. Fatuzzo, S. Moser, M. Kim, R. Fittipaldi, A. Vecchione, V. Granata, Y. Sassa, F. Cossalter, G. Gatti, M. Grioni, H. M. Rønnow, N. C. Plumb, C. E. Matt, M. Shi, M. Hoesch, T. K. Kim, T.-R. Chang, H.-T. Jeng, C. Jozwiak *et al.*, Hallmarks of Hunds coupling in the Mott insulator Ca_2RuO_4, Nat. Commun. **8**, 15176 (2017).

[47] H. U. R. Strand, M. Zingl, N. Wentzell, O. Parcollet, and A. Georges, Magnetic response of Sr_2RuO_4: Quasi-local spin fluctuations due to Hund's coupling, Phys. Rev. B **100**, 125120 (2019).

[48] H. Suzuki, L. Wang, J. Bertinshaw, H. U. R. Strand, S. Käser, M. Krautloher, Z. Yang, N. Wentzell, O. Parcollet, F. Jerzembeck, N. Kikugawa, A. P. Mackenzie, A. Georges, P. Hansmann, H. Gretarsson, and B. Keimer, Distinct spin and orbital dynamics in Sr_2RuO_4, Nat. Commun. **14**, 7042 (2023).

[49] A. Hunter, S. Beck, E. Cappelli, F. Margot, M. Straub, Y. Alexanian, G. Gatti, M. D. Watson, T. K. Kim, C. Cacho, N. C. Plumb, M. Shi, M. Radovic, D. A. Sokolov, A. P. Mackenzie, M. Zingl, J. Mravlje, A. Georges, F. Baumberger, and A. Tamai, The fate of quasiparticles at high-temperature in the correlated metal Sr_2RuO_4, Phys. Rev. Lett. **131**, 236502 (2023).

[50] G. D. Mahan, *Many-Particle Physics* (Springer US, New York, NY, 2000).

[51] A. Khurana, Electrical conductivity in the infinite-dimensional Hubbard model, Phys. Rev. Lett. **64**, 1990 (1990).

[52] B. S. Shastry and B. I. Shraiman, Raman scattering in Mott-Hubbard systems, Int. J. Mod. Phys. B **05**, 365 (1991).

[53] J. R. Yates, X. Wang, D. Vanderbilt, and I. Souza, Spectral and Fermi surface properties from Wannier interpolation, Phys. Rev. B **75**, 195121 (2007).

[54] D. Destraz, L. Das, S. S. Tsirkin, Y. Xu, T. Neupert, J. Chang, A. Schilling, A. G. Grushin, J. Kohlbrecher, L. Keller, P. Puphal, E. Pomjakushina, and J. S. White, Magnetism and anomalous

transport in the Weyl semimetal pralge: Possible route to axial gauge fields, npj Quantum Mater. **5**, 5 (2020).

[55] S. S. Tsirkin, High performance Wannier interpolation of Berry curvature and related quantities with Wannier-Berri code, npj Comput. Mater. **7**, 33 (2021).

[56] J. K. Freericks, T. P. Devereaux, and R. Bulla, Exact theory for electronic Raman scattering of correlated materials in infinite dimensions, Phys. Rev. B **64**, 233114 (2001).

[57] C. Berthod, J. Mravlje, X. Deng, R. Žitko, D. van der Marel, and A. Georges, Non-Drude universal scaling laws for the optical response of local Fermi liquids, Phys. Rev. B **87**, 115109 (2013).

[58] J.-C. Philippe, Ph.D. thesis, Université de Paris, 2021.

[59] Y. Aiura, Y. Yoshida, I. Hase, S. I. Ikeda, M. Higashiguchi, X. Y. Cui, K. Shimada, H. Namatame, M. Taniguchi, and H. Bando, Kink in the dispersion of layered strontium ruthenates, Phys. Rev. Lett. **93**, 117005 (2004).

[60] N. J. C. Ingle, K. M. Shen, F. Baumberger, W. Meevasana, D. H. Lu, Z.-X. Shen, S. Nakatsuji, Z. Q. Mao, Y. Maeno, T. Kimura, and Y. Tokura, Quantitative analysis of Sr_2RuO_4 angle-resolved photoemission spectra: Many-body interactions in a model Fermi liquid, Phys. Rev. B **72**, 205114 (2005).

[61] A. Horvat, R. Žitko, and J. Mravlje, Non-Fermi-liquid fixed point in multi-orbital Kondo impurity model relevant for Hund's metals, arXiv:1907.07100.

[62] Y. Wang, E. Walter, S.-S. B. Lee, K. M. Stadler, J. von Delft, A. Weichselbaum, and G. Kotliar, Global phase diagram of a spin-orbital Kondo impurity model and the suppression of Fermi-liquid scale, Phys. Rev. Lett. **124**, 136406 (2020).

[63] E. Walter, K. M. Stadler, S.-S. B. Lee, Y. Wang, G. Kotliar, A. Weichselbaum, and J. von Delft, Uncovering non-Fermi-liquid behavior in Hund metals: Conformal field theory analysis of an SU(2) × SU(3) spin-orbital Kondo model, Phys. Rev. X **10**, 031052 (2020).

[64] ARPES spectra at ∼80 meV binding energy appear consistent with this nesting property (A. Tamai, private communication).

[65] S. J. Youn, B. I. Min, T. H. Rho, and K. S. Kim, Nested Fermi surfaces, optical peaks, and laser-induced structural transition in Al, Phys. Rev. B **69**, 033101 (2004).

[66] B. S. Shastry and B. I. Shraiman, Theory of Raman scattering in Mott-Hubbard systems, Phys. Rev. Lett. **65**, 1068 (1990).

[67] P. B. Allen, Electron self-energy and generalized Drude formula for infrared conductivity of metals, Phys. Rev. B **92**, 054305 (2015).

[68] H. T. Dang, J. Mravlje, A. Georges, and A. J. Millis, Band structure and terahertz optical conductivity of transition metal oxides: Theory and application to $CaRuO_3$, Phys. Rev. Lett. **115**, 107003 (2015).

[69] N. Lin, E. Gull, and A. J. Millis, Physics of the pseudogap in eight-site cluster dynamical mean-field theory: Photoemission, Raman scattering, and in-plane and *c*-axis conductivity, Phys. Rev. B **82**, 045104 (2010).

[70] E. Gull and A. J. Millis, Superconducting and pseudogap effects on the interplane conductivity and Raman scattering cross section in the two-dimensional Hubbard model, Phys. Rev. B **88**, 075127 (2013).

[71] A. Kowalski, A. Hausoel, M. Wallerberger, P. Gunacker, and G. Sangiovanni, State and superstate sampling in hybridization-expansion continuous-time quantum Monte Carlo, Phys. Rev. B **99**, 155112 (2019).

[72] N. Wentzell, H. U. Strand, S. Kaeser, Yann In 'T Veld, D. Simon, A. Hampel, Malte-Roesner, Egcpvanloon, O. Parcollet, O. Gingras, D. Philipp, T. Hahn, and M. Zingl, TRIQS/TPRF: Version 3.2.1 (2023).

[73] E. G. C. P. van Loon and H. U. R. Strand, Dual Bethe-Salpeter equation for the multi-orbital lattice susceptibility within dynamical mean-field theory, arXiv:2306.05157.